

Acid Etching-Driven Self-Assembly of Mn-Shell Inducing Rock-Salt Phase for Enhanced Single-Crystal Ni-Rich Cathodes

Xiaotu Ma,^[a] Zifei Meng,^[a] Jiahui Hou,^[a] Zeyi Yao,^[a] Zexin Wang,^[a] Fulya Dogan,^[b] Zhenzhen Yang,^[b] Maksim Sultanov,^[c, e] Guanhui Gao,^[d] Hua Guo,^[d] Yimo Han,^[d] Jianguo Wen,^[c] and Yan Wang*^[a]

With the wide adoption of Li-ion batteries, Ni-rich cathode is considered as one of the most promising candidates of cathodes due to its high energy density and low cost. However, stability decreased with increasing Ni content in the Ni-rich cathode. To solve this bottleneck, many strategies, such as coating, doping, surface modification, and special morphologies, have been developed. Herein, we introduce a groundbreaking approach for enhancing Ni-rich cathode through an innovative acid etching process that promotes Mn shell self-assembly, inducing a rock-salt phase on the surface. This method not only simplifies the Ni-rich cathode modification process, but also significantly improves the structural stability and electrochemical performance of Ni-rich cathode. Our

findings demonstrate that developed single-crystal Ni-rich cathode shows 3–34% better stability compared to both commercial modified Ni-rich cathode and unmodified counterparts. The unique Mn shell effectively mitigates reversible phase shifts during cycling, contributing to a remarkable enhancement in cycling stability. This novel fabrication technique paves the way for cost-effective production of high-performance cathode materials, offering substantial benefits for lithium-ion battery technology. And this study proves the potential of this method in advancing the design and development of durable, high-capacity cathode materials for next-generation batteries.

Introduction

With the rapid development of battery technology, Li-ion batteries (LIBs) have found extensive applications in portable electronics, electric vehicles, and energy storage facilities. For a superior user experience, the energy density and lifespan of LIBs must be enhanced, which are limited by the low discharge capacity of cathode materials compared to anode materials.^[1] Among many cathode candidates, including lithium cobalt oxide (LiCoO_2 , LCO), lithium manganese oxide (LiMn_2O_4 , LMO), lithium iron phosphate (LiFePO_4 , LFP), lithium nickel manganese cobalt oxide ($\text{LiNi}_x\text{Mn}_{1-x}\text{Co}_{1-y}\text{O}_2$, NMC), and lithium nickel cobalt

aluminum oxide ($\text{LiNi}_x\text{Co}_y\text{Al}_{1-x-y}\text{O}_2$, NCA), Ni-rich NMC ($x > 0.5$) cathode is considered one of the most promising cathodes because of its high discharge capacity, low cost, and high working potential.^[2] Traditionally, the NMC cathodes are spherical polycrystal particles synthesized by co-precipitation reactions and subsequent solid sintering. Unfortunately, these particles tend to crack along grain boundaries during cycling, especially because of the significant lattice collapse at high delithiation states.^[1,2] This issue intensifies with an increase in Ni content, causing rapid capacity deterioration and structural degradation of the Ni-rich NMC cathode.

Several innovative strategies,^[3] like coating,^[4] doping,^[5] surface modification,^[6] core-shell,^[7] and concentration-gradient,^[4a,7a,8] have been pursued to address these challenges. Recently, single-crystal NMC has emerged as a noteworthy solution, since it is boundary-free configuration, which can effectively reduce cracks, leading to a significant improvement in stability and electrochemical performance. In addition, for better results, combining strategies such as single-crystal techniques with coating^[9] or doping^[10] offers potential for mitigating cracks, reducing phase transformation, and prolonging the cycle life, which also stimulates researchers' interests. Moreover, the surface construction also shows good effects on improving stability and electrochemical performance for Ni-rich NMC cathode. Huang et al.^[11] and Chen et al.^[12] reported spinel phase coating on the layered Ni-rich cathode materials to enhance cycling stability. And a strategy using Mn ions to induce spinel structure coating on the Ni-rich cathode was reported by Zhang

[a] X. Ma, Z. Meng, J. Hou, Z. Yao, Z. Wang, Y. Wang

Department of Mechanical and Materials Engineering, Worcester Polytechnic Institute, 100 Institute Road, Worcester, MA 01609, USA
E-mail: yanwang@wpi.edu

[b] F. Dogan, Z. Yang

Chemical Sciences and Engineering Division, Argonne National Laboratory, 9700 S Cass Ave, Lemont, IL 60439, USA

[c] M. Sultanov, J. Wen

Center for Nanoscale Materials, Argonne National Laboratory, 9700 S Cass Ave, Lemont, IL 60439, USA

[d] G. Gao, H. Guo, Y. Han

Department of Materials Science and Nanoengineering, Rice University, 6100 Main St, Houston, TX 77005, USA

[e] M. Sultanov

Northern Illinois University, Department of Physics, 1425 W. Lincoln Hwy, DeKalb, IL 60115

 Supporting information for this article is available on the WWW under <https://doi.org/10.1002/batt.202400501>

et. al.^[13] Zhang et al.^[14] reported spinel/rock salt phases coated Ni-rich cathode with superior stability.

Here, we develop the concepts of single-crystal formation with Mn self-coating. We have previously reported a universal etching method to fabricate single-crystal NMC 111 and 622.^[2] Impressively, when this method is applied to 83Ni (an NMC cathode with an 83% Ni concentration, 6% Mn, and 11% Co), a distinct phenomenon unfolds. During etching, Mn is first leached into the solution, only to re-precipitate onto the powder, forming a protective Mn coating shell and inducing a rock-salt phase at the surface. The obtained single-crystal 83Ni cathode exhibits a discharge capacity of 203.2 mAh/g with an initial coulombic efficiency (ICE) of 91.99%. It demonstrates superior stability, ranging from 2.7%–47.4% better than control samples, including various commercial Ni-rich NMC cathodes and the pristine 83Ni cathode. This enhanced stability during cycling is attributed to the Mn shell, which improves the reversible phase transformation. This process eliminates the need for introducing other elements as coatings or dopants and avoids the mixing process, thereby reducing the cost of modifications for Ni-rich single-crystal cathodes. It pioneers a novel single-crystal fabrication technique while introducing a reliable self-coating Mn cathode production method, avoiding the need for added chemicals in sintering phases. Additionally, it can be integrated with direct recycling processes to regenerate high-performance Ni-rich single-crystal cathodes.

Results and Discussion

The pristine-83Ni cathode was first prepared via a coprecipitation reaction and heat treatment process without any coating or doping and its morphology was shown in Figure S1. The pristine-83Ni was then dispersed in the diluted H₂SO₄ under room temperature for a different etching time from 1 h–25 h. As illustrated in Figure 1a–f, the pristine-83Ni was converted from polycrystalline to single-crystalline as the etching time increased and the layered structure collapsed in the meantime (Figure 1g). This phenomenon is similar to our previous work,^[2] but the cracking started earlier than that of NMC111 and NMC622. After 15 h etching, almost all polycrystal particles were successfully converted to single-crystalline particles. Based on the ICP results of leaching solution in Figure 1h, the transition metals were leaching out at the same rate at the first 5 h, while the amount of Li in the leaching solution increased dramatically in the first 5 h, which was totally leached out after 25 h etching. Interestingly, the Mn started to precipitate starting from 5 h and all Mn precipitated at around 15 h. Due to the precipitation of Mn, the Ni content in the etched powder decreased, but it was still close to 80% (Table S1). However, for 25 h etching process, almost all Li could be leached out, which is 40% more than that for NMC111.

To further elucidate the Mn self-coating process, TEM and XPS were utilized. The EDS mapping measurement of an individual single-crystal 83Ni particle was investigated to detect the transition metals distribution in Figure 2a, indicating a clear Mn shell in yellow color. However, the Mn shell is not very

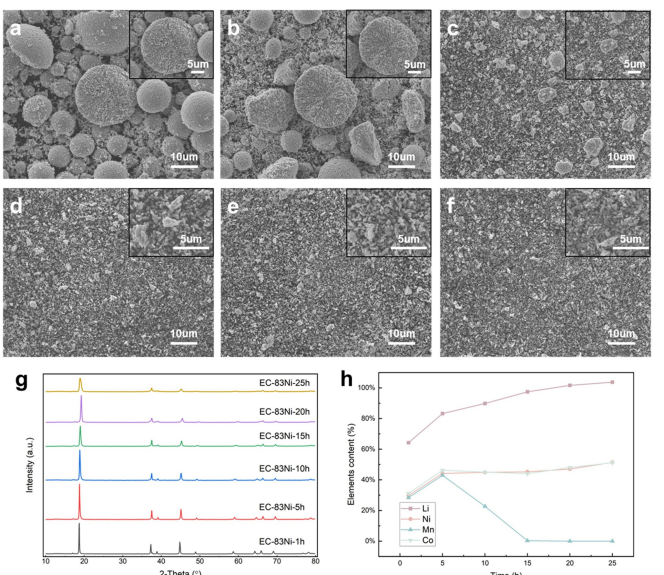


Figure 1. Morphology, structure, and elements content changes during etching process. SEM images of (a) EC-83Ni-1 h; (b) EC-83Ni-5 h; (c) EC-83Ni-10 h; (d) EC-83Ni-15 h; (e) EC-83Ni-20 h; (f) EC-83Ni-25 h; XRD patterns comparison of all etched samples (g); the elements content change in the etching solution following the etching time (h).

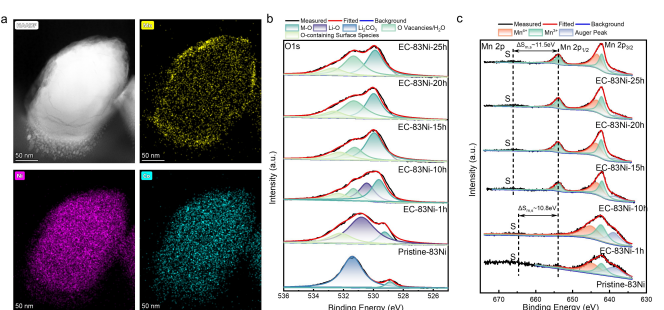


Figure 2. Chemical environments analysis. (a) HAADF-STEM image and EDS mapping images of EC-83Ni-25 h; (b) XPS patterns of O1s for pristine-83Ni and etched 83Ni with different etching time; (c) XPS patterns of Mn2p for pristine-83Ni and etched 83Ni with different etching time.

uniform, which is likely due to the increased surface area and low precipitated amount. Figure 2b presents the O1s spectra, which include several peaks: Li–O peak at approximately 530.8 eV,^[15] CO₃ from Li₂CO₃ at 531.4 eV,^[16] metal–oxygen (M–O) bond around 529 eV,^[17] O vacancies/H₂O near 531 eV,^[18] and O-containing surface species at about 532 eV.^[18] Notably, only Pristine-83Ni exhibits the Li₂CO₃ peak, as surface Li₂CO₃ can be removed by water and acid during the etching process, consistent with the disappeared surface Li peak at 55.3 eV^[19] in Li1s spectra of Figure S2a. In EC-83Ni-1 h, the Li₂CO₃ is absent, and approximately 30 mol% of Li has been leached out (as shown in Figure 1h), leaving behind Li in the form of Li–O bonds. After 15 hours of etching, all Li is leached out, as evidenced by the disappearance of the Li–O bond peak, consistent with the Li 1s spectra in Figure S2a where lattice Li peak at 54 eV^[19] vanishes with increasing etching time.

Another significant observation is the peak shift of M–O, attributable to Li leaching and Mn precipitation. During the first hour of etching, the M–O peak shifts from 528.9 eV–529.2 eV, and after 15 hours of etching, this peak shifts to ~530 eV, indicating the increased content of the MnO_2 shell on the surface where MnO_2 is around 529–530 eV.^[20] This phenomenon is further corroborated by Mn 2p spectra in Figure 2c, and Ni 2p and Co 2p spectra in Figure S2b and S2c. The Mn 2p peaks become stronger and sharper with increased etching time, suggesting that Mn re-precipitates on the surface, thereby covering the signal of Ni and Co, particularly the satellite peaks of Mn which become more obvious as the etching progresses. Additionally, the fitting results suggest that Mn is more likely in the 4+ state (642.3 and 654.2 eV^[21]). And the satellite structure is positioned at ~10.8 eV from the main Mn 2p1/2 emission in Pristine-83Ni and EC-83Ni-1 h, and at ~11.5 eV in EC-83Ni-15 h/20 h/25 h, indicating a high valence than 3+ (641.8 and 654.2 eV^[21]).^[22]

The mechanism of Mn precipitation during acid treatment has been widely reported,^[20a] which is related to the development of new materials by solid-state chemistry, focusing on the preparation of new metastable MnO_2 compounds by acid delithiation of the stable LiMn_2O_4 and Li_3MnO_3 phases.^[23] Compared to the work reported by Billy et al.,^[20a] Ni-rich cathode materials exhibited a faster dissolution and Mn precipitation process than NMC111 and it can be observed in most acid etching processes (Table S2).

To confirm the etching mechanism, solid-state NMR was employed to investigate the chemical environment change during the etching process in Figure 3. ${}^6\text{Li}$ NMR quantitatively compares the structural lithium shown in Figure 3a. Lithium environments in pristine Ni rich NMC cathodes generally give peaks around 600 ppm. This large shift is due to the hyperfine interaction between lithium nuclear spin and the unpaired electrons of paramagnetic transition metal ions and can be assigned to Li in lithium layers. The narrow peak at 0 ppm corresponds to lithiums in diamagnetic region, is attributed to surface lithium impurities. With etching, it is clearly seen that

the lithium is gradually removed from the structure (bulk lithium is in the yellow square and surface lithium is in the green square) and with 25 h etching there is almost no structural lithium left. As the etching time increases the main bulk peak shifts to lower frequencies due to formation of undercoordinated lithium sites, vacancies, and oxidation state changes in TM as lithium is removed from the structure. ${}^2\text{H}$ NMR in Figure 3b investigates possible H ions insertion and H/Li exchange. Impurities and surface H environments should give peaks around 0 ppm (orange color) whereas any structural H coordinated to Mn or Ni should give shifted peaks due to hyperfine shift (in blue color) where other peaks are spinning sidebands. With short etching time no significant H insertion is observed and as the time increased to 25 h, there is a new peak formation, signature to proton insertion.

Considering the good single-crystal morphology and layered structure of the obtained single-crystal cathode, EC-83Ni-25 h was utilized to synthesize the cathode material (SC-83Ni-25 h). Figure 4a shows the morphology of SC-83Ni-25 h is still single crystal after sintering and the particle size distribution is under microlevel. Figure 4b and Figure S3 present the XRD and XRD refinement results of SC-83Ni-25 h and Pristine-83Ni. Both samples exhibited a well layered structure and there are no peaks of Mn-based materials observed in SC-83Ni-25 h, which is because of the low content of Mn shell. Normally, the peaks can be detected when the Mn shell content is over 5%.^[24] The ICP results in Table S2 show that if all Mn precipitated as Mn shell, the content of Mn shell would be 4 mol%, which is under the detective limitation. Therefore, only a layered structure with a $R\bar{3}m$ space group is added in Rietveld refinements. Based on the refinement results in Table S3, SC-83Ni-25 h has comparable lattice parameters. And the $\text{Li}^+/\text{Ni}^{2+}$ cation mixing in the layered structure of the Ni-rich component within SC-83Ni-25 h is determined to be 1.12%, lower than 3.37% in Pristine-83Ni. Notably, the Mn shell increases the c/a ratio in the layered structure (Table S3), indicating the significant coating effect on improving the structural ordering of coated Ni-rich single crystal materials through the self-assembly of the Mn shell during acid etching process. ${}^6\text{Li}$ NMR spectra comparison of Pristine-83Ni and SC-83Ni-25 h demonstrates a similar peak shape for both samples in Figure 4c. In Figure 4d, the STEM HAADF images detected rock-salt phase, mixed phase of rock-salt, spinel and

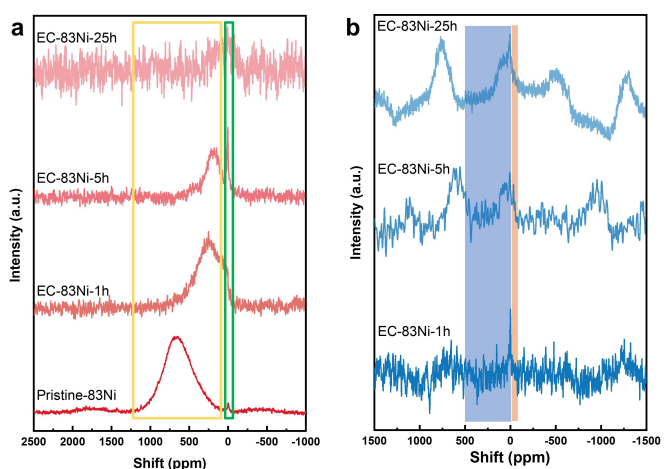


Figure 3. Solid-state NMR spectra studies of pristine and etched 83Ni samples. (a) ${}^6\text{Li}$ NMR spectra; (b) ${}^2\text{H}$ NMR spectra.

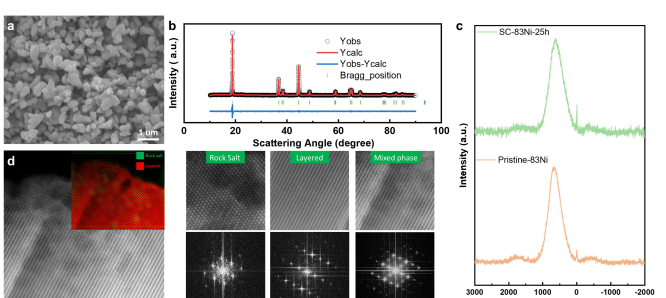


Figure 4. Physical properties evaluation of SC-83Ni-25 h. (a) SEM image of SC-83Ni-25 h; (b) XRD refinement of SC-83Ni-25 h; (c) ${}^6\text{Li}$ solid-state NMR comparison between Pristine-83Ni and SC-83Ni-25 h; (d) STEM HAADF images and magnifications of SC-83Ni-25 h.

layered phases, and layered phase from surface to bulk as shown in magnifications of layered area, rock-salt area and mixed area, which enhances the binding between the host and the surface layer and mitigates the volume mismatch issue.^[13] However, as shown in Figure S4, there are fewer rock-salt and mixed phases on the surface of the SC-83Ni-15 h, which was sintered under the same calcination conditions as SC-83Ni-25 h. This difference is due to the shorter etching time, indicating that the change in surface phases is caused by the etching process and the Mn shell. In addition, STEM-EDS mapping and linear mapping images show a ~10 nm thick of Mn shell in Figure S5.

The electrochemical performance of SC-83Ni-25 h was tested using lithium half-cells in standard 2032 coin cells. Commercial 811, Commercial 83Ni and Pristine 83Ni are chosen as control counterparts, because Commercial 811 has the similar composition to SC-83Ni after etching and Commercial 83Ni and Pristine 83Ni have the same composition as SC-83Ni-25 h before etching. Figure 5a presents the initial charge-discharge curves of all samples at 0.05 C. All control samples show a discharge capacity of about 212.7 mAh/g with an initial coulombic efficiency (ICE) of around 90.7% and SC-83Ni-25 h exhibits a discharge capacity of 203.2 mAh/g with an ICE of 91.99%. The lower discharge capacity is caused by the rock-salt phase coating layer.^[24,25] Although SC-83Ni-25 h has a slightly lower discharge capacity under 0.05 C compared to control samples, it shows a higher capacity under a higher C-rate in Figure 5b. Especially, SC-83Ni-25 h demonstrated a comparable discharge capacity as Commercial 811, which is over 10 mAh/g better than Commercial 83Ni and Pristine 83Ni. Figure 5c illustrates the discharge of materials at various current densities

after the same various rates charge and hold until the current is lower than 0.02 C. SC-83Ni-25 h still discharges to 80% of its 0.1 C discharge capacity under 5 C, which is comparable to Commercial 811 and presents significant potential in fast charging (15 min to 80% state of charge). Figures 5d and 5e show the Li diffusion coefficient comparison between control samples and SC-83Ni-25 h during charging and discharging under 0.1 C, which is based on the GITT shown in Figure S6. At the charging process, all samples share a similar trend of the Li diffusion coefficients change with comparable Li diffusion coefficients. At the beginning of the discharging process, all samples exhibit a similar trend and Li diffusion coefficients. However, SC-83Ni-25 h exhibits a lower Li diffusion coefficient at the end of the discharging process compared to control samples, which is because of the rock-salt phase coating layer. Figure 5f demonstrates the resistance calculated from GITT, which shows comparable resistance and trend of all samples during charging and discharging processes. It means that SC-83Ni-25 h reaches commercial quality on rate performance, Li diffusion coefficients and resistance. Considering that commercial Ni-rich cathode materials always have coating or doping materials, leading to better rate performance, higher Li diffusion coefficients and lower resistance, SC-83Ni-25 h without any extra coating or doping elements proves its potential to utilize in particle applications.

SC-83Ni-25 h also demonstrates improved stability. Figure 6a presents that SC-83Ni-25 h still has 155.2 mAh/g after 200 cycles under 0.5 C, which is higher than Commercial 811 (151.2 mAh/g), Commercial 83Ni (110.2 mAh/g), and Pristine 83Ni (65.6 mAh/g). After 200 cycles, SC-83Ni-25 h exhibits a capacity retention of 81.4% in Figure 6b, which is higher than

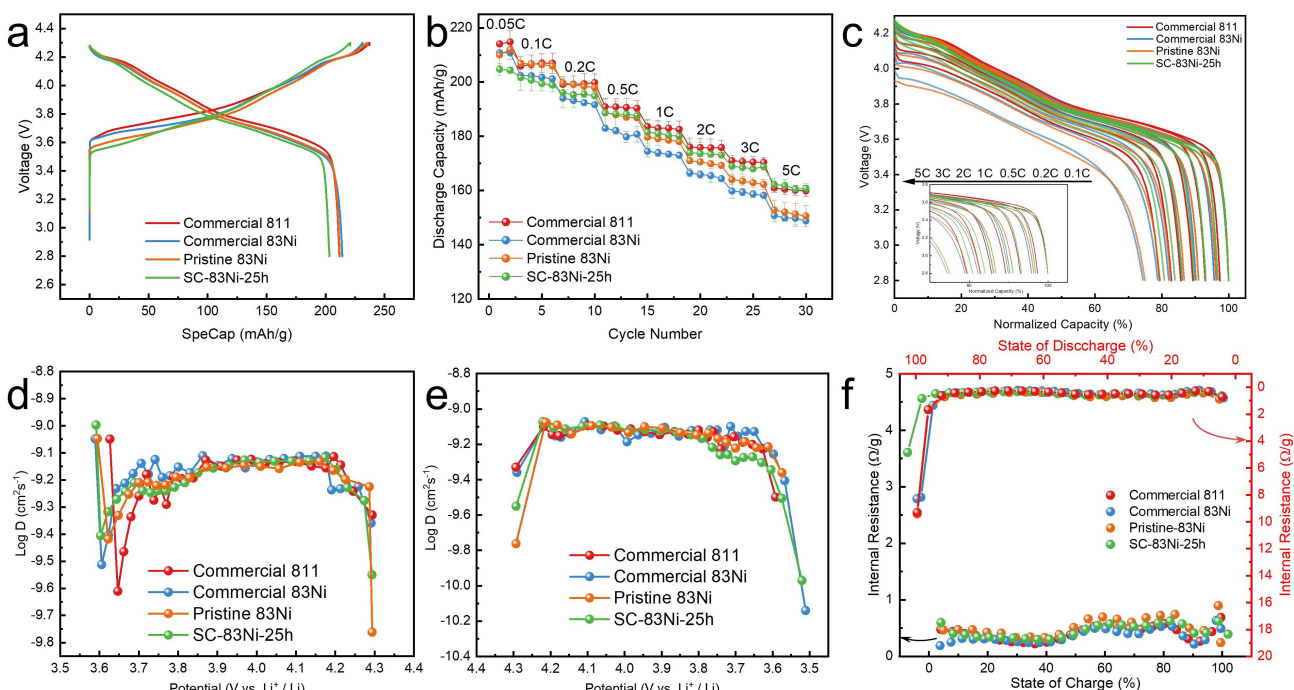


Figure 5. Electrochemical performance comparison between SC-83Ni-25 h and various control samples. (a) first-cycle voltage profile comparison; (b, c) half cells rate performance comparison; (d, e) lithium diffusion coefficients calculated from GITT for SC-83Ni-25 h and various control samples; (f) internal resistance caculated from GITT for SC-83Ni-25 h and various control samples.

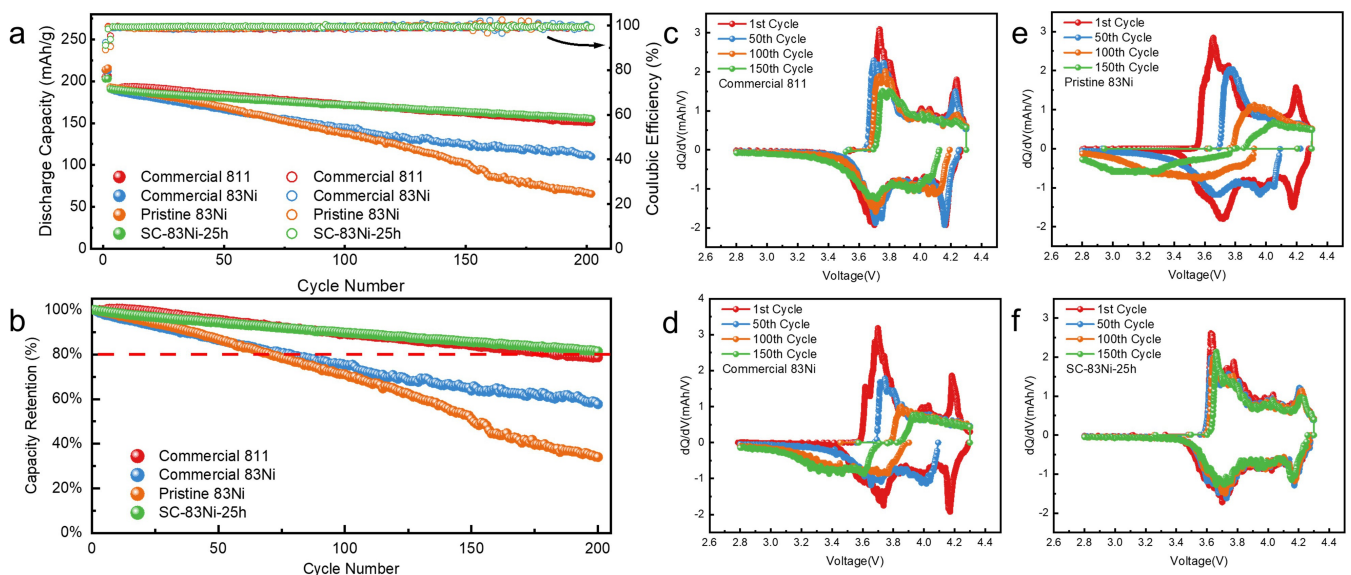


Figure 6. Cycling stability comparison between SC-83Ni-25 h and various control samples. (a, b) cycling performance comparison between SC-83Ni-25 h and various control samples; dQ/dV curves at different cycles of Commercial 822 (c), Commercial 83Ni (d), Pristine 83Ni (e), and SC-83Ni-25 h (f).

that of Commercial 811 (78.7%), Commercial 83Ni (57.7%) and Pristine 83Ni (34.0%). Figure S7 shows the MedVoltage change during cycling, where SC-83Ni-25 h is much more stable than all control samples. The more stable MedVoltage indicates more stable phase stability, which is confirmed by CV curves in Figure S8 and dQ/dV curves during cycling in Figures 6c–6f. All control samples show similar CV curves, but the CV curve of SC-83Ni-25 h exhibits significantly less phase transformation compared to all control samples. In Figures 6c–6f, it is obvious that after 150 cycles, SC-83Ni-25 h kept almost the same structure as the beginning, followed by Commercial 811 and Commercial 83Ni, and Pristine 83Ni is the worst. The serious structure collapse of Pristine 83Ni after cycling is due to no modification. The better structure collapse of Commercial 811 and Commercial 83Ni is benefited by their coating or doping. The EIS spectra in Figure S9 exhibits that SC-83Ni-25 h has the lowest impedance compared to all control samples, which is consistent with previous results.

Conclusions

In conclusion, this study has successfully developed a novel production process for single-crystal Ni-rich cathodes, utilizing an innovative acid etching method that prompts Mn self-assembly to form a coating. This approach yields cathode materials that not only match but, in certain aspects, surpass the electrochemical performance of the best available commercial equivalents. Notably, the cycling stability of these cathodes shows a remarkable improvement of 47.4% over Pristine 83Ni and a 2.7% enhancement compared to the commercial 811 counterpart, which is benefited by the self-assembly Mn shell. These advancements signify that our process can reliably generate single-crystal Ni-rich cathode materials with superior

performance. Moreover, the method avoids the need for additional coating or doping agents, thereby simplifying the production process and reducing costs significantly. It also transitions the cathode structure from polycrystalline to single-crystal, further contributing to economic and procedural efficiency. While there is a minor drawback of Li and transition metal loss in the etching solution, we have demonstrated that these can be effectively recovered and reused via solvent extraction, precipitation, or as inputs for new cathode synthesis. Additionally, optimizing the liquid-to-solid ratio can mitigate these losses and precisely control the Mn coating amount. We also assume that the mechanism of Mn leaching and precipitation could be advantageously leveraged in the recycling sector for selective material recovery, as it is inherently compatible with established hydrometallurgical processes. The potential for this technique extends beyond production, promising to introduce significant improvements in the sustainability and economics of cathode material recycling.

Acknowledgements

This work was performed through the ReCell Center, which gratefully acknowledge the support from the U.S. Department of Energy (DOE), Office of Energy Efficiency and Renewable Energy, and the Vehicle Technologies Office. XPS work was conducted at the Post Test Facility of Argonne National Laboratory, operated for DOE Office of Science by UChicago Argonne, LLC, under contract no. DE-AC02-06CH11357.

Conflict of Interests

The authors declare no conflict of interest.

Data Availability Statement

The data that support the findings of this study are available on request from the corresponding author. The data are not publicly available due to privacy or ethical restrictions.

Keywords: Acid etching • Ni-rich cathode • Single-crystal cathode • Manganese coating

- [1] H. Zhang, X. He, Z. Chen, Y. Yang, H. Xu, L. Wang, X. He, *Adv. Energy Mater.* **2022**, *12*, 2202022.
- [2] X. Ma, P. Vanaphuti, J. Fu, J. Hou, Y. Liu, R. Zhang, S. Bong, Z. Yao, Z. Yang, Y. Wang, *Nano Energy* **2021**, *87*, 106194.
- [3] J. Kim, H. Lee, H. Cha, M. Yoon, M. Park, J. Cho, *Adv. Energy Mater.* **2018**, *8*, 1702028.
- [4] a) P. Hou, J. Yin, M. Ding, J. Huang, X. Xu, *Small* **2017**, *13*, 1701802; b) X. Zeng, C. Zhan, J. Lu, K. Amine, *Chem* **2018**, *4*, 690–704.
- [5] a) W. Liu, P. Oh, X. Liu, M. J. Lee, W. Cho, S. Chae, Y. Kim, J. Cho, *Angew. Chem. Int. Ed. Engl.* **2015**, *54*, 4440–4457; b) A. Kitajou, J. Yoshida, S. Nakanishi, S. Okada, J.-i. Yamaki, *J. Power Sources* **2013**, *244*, 658–662.
- [6] a) L. Liu, M. Li, L. Chu, B. Jiang, R. Lin, X. Zhu, G. Cao, *Prog. Mater. Sci.* **2020**, *111*, 100655; b) Y.-G. Zou, F. Meng, D. Xiao, H. Sheng, W.-P. Chen, X.-H. Meng, Y.-H. Du, L. Gu, J.-L. Shi, Y.-G. Guo, *Nano Energy* **2021**, *87*, 106172.
- [7] a) P. Hou, H. Zhang, Z. Zi, L. Zhang, X. Xu, *J. Mater. Chem. A* **2017**, *5*, 4254–4279; b) N. Phattharasupakun, J. Wuttiprom, S. Duangdangchote, S. Sarawutanukul, C. Tomon, F. Duriyasart, S. Tubtimkuna, C. Aphirakarawong, M. Sawangphruk, *Energy Storage Mater.* **2021**, *36*, 485–495.
- [8] W. Chen, Y. Li, J. Zhao, F. Yang, J. Zhang, Q. Shi, L. Mi, *RSC Adv.* **2016**, *6*, 58173–58181.
- [9] a) J. Shen, B. Zhang, A. Dai, X. He, Z. Xiao, L. Yu, T. Li, J. Wen, X. Li, T. Liu, X. Ou, K. Amine, *J. Power Sources* **2023**, *559*, 232653; b) Y. Lu, X. Zeng, J. Wang, L. Yang, S. Hu, C. Jia, H. Zhao, D. Yin, X. Ge, X. Xi, *Adv. Mater. Interfaces* **2019**, *6*, 1901368.
- [10] X. Ou, T. Liu, W. Zhong, X. Fan, X. Guo, X. Huang, L. Cao, J. Hu, B. Zhang, Y. S. Chu, G. Hu, Z. Lin, M. Dahbi, J. Alami, K. Amine, C. Yang, J. Lu, *Nat. Commun.* **2022**, *13*, 2319.
- [11] X. Huang, W. Zhu, J. Yao, L. Bu, X. Li, K. Tian, H. Lu, C. Quan, S. Xu, K. Xu, Z. Jiang, X. Zhang, L. Gao, J. Zhao, *J. Mater. Chem. A* **2020**, *8*, 17429–17441.
- [12] X. Chen, Y. Tang, C. Fan, S. Han, *Electrochim. Acta* **2020**, *341*, 136075.
- [13] J. Zhang, Z. Yang, R. Gao, L. Gu, Z. Hu, X. Liu, *ACS Appl. Mater. Interfaces* **2017**, *9*, 29794–29803.
- [14] X. Zhang, M. Wang, Z. Guo, C. Chen, Y.-J. Cheng, Y. Xia, *Energy Mater. Adv.* **2023**, *4*, 0034.
- [15] K. N. Wood, G. Teeter, *ACS Appl. Energ. Mater.* **2018**, *1*, 4493–4504.
- [16] E. Björklund, D. Brandell, M. Hahlén, K. Edström, R. Younesi, *J. Electrochem. Soc.* **2017**, *164*, A3054.
- [17] X. Ma, M. Chen, Z. Zheng, D. Bullen, J. Wang, C. Harrison, E. Gratz, Y. Lin, Z. Yang, Y. Zhang, F. Wang, D. Robertson, S.-B. Son, I. Bloom, J. Wen, M. Ge, X. Xiao, W.-K. Lee, M. Tang, Q. Wang, J. Fu, Y. Zhang, B. C. Sousa, R. Arsenault, P. Karlson, N. Simon, Y. Wang, *Joule* **2021**, *5* (11), 2955–2970.
- [18] T. J. Frankcombe, Y. Liu, *Chem. Mater.* **2023**, *35*, 5468–5474.
- [19] D. Pritzl, T. Teufel, A. T. S. Freiberg, B. Strehle, J. Sicklinger, H. Sommer, P. Hartmann, H. A. Gasteiger, *J. Electrochem. Soc.* **2019**, *166*, A4056–A4066.
- [20] a) E. Billy, M. Joulie, R. Laucournet, A. Boulineau, E. De Vito, D. Meyer, *ACS Appl. Mater. Interfaces* **2018**, *10*, 16424–16435; b) L. Yuan, X.-H. Lu, X. Xiao, T. Zhai, J. Dai, F. Zhang, B. Hu, X. Wang, L. Gong, J. Chen, C. Hu, Y. Tong, J. Zhou, Z. L. Wang, *ACS Nano* **2012**, *6*, 656–661.
- [21] Y. Zhang, Z.-B. Wang, F.-D. Yu, L.-F. Que, M.-J. Wang, Y.-F. Xia, Y. Xue, J. Wu, *J. Power Sources* **2017**, *358*, 1–12.
- [22] G. Cherkashinin, K. Nikolowski, H. Ehrenberg, S. Jacke, L. Dimesso, W. Jaegermann, *Phys. Chem. Chem. Phys.* **2012**, *14*, 12321–12331.
- [23] a) J. C. Hunter, *J. Solid State Chem.* **1981**, *39*, 6; b) M. M. Thackeray, P. J. Johnson, L. A. de Picciotto, P. G. Bruce, J. B. Goodenough, *Mater. Res. Bull.* **1984**, *19*, 179–187.
- [24] H. Xue, Z. Wenchang, Y. Junyi, B. Liangmin, L. Xiangyi, T. Kai, L. Hui, Q. Chuxuan, X. Shiguo, X. Kaihua, J. Zhenkang, Z. Xiang, G. Lijun, Z. Jianqing, *J. Mater. Chem. A* **2020**, *8*, 17429–17441.
- [25] X. Dong, J. Yao, W. Zhu, X. Huang, X. Kuai, J. Tang, X. Li, S. Dai, L. Shen, R. Yang, L. Gao, J. Zhao, *J. Mater. Chem. A* **2019**, *7*, 20262–20273.

Manuscript received: July 26, 2024

Accepted manuscript online: September 28, 2024

Version of record online: November 7, 2024